Pergamon

Int. J. Heat Mass Transfer. Vol. 40, No. 9, pp. 1993–2007, 1997

0017–9310/97 $17.00+0.00

PII: S0017–9310(96)00305–5

Heat transfer and solidification in planar-flow melt-spinning: high wheelspeeds

J. K. CARPENTER
Rohm and Haas Company, P.O. Box 219, Bristol, PA 19007, U.S.A.

and

P. H. STEEN†
School of Chemical Engineering, Cornell University, Ithaca, NY 14850, U.S.A.

(*Received* 8 *February* 1996 *and in final form* 26 *August* 1996)

Abstract—Operation of the planar-flow melt-spinning process in a regime where the wheelspeed is high relative to the (average) solidification rate is studied. A distinct solidification front occurs. An analysis based on the governing energy and momentum equations shows that heat transfer and solidification are only weakly coupled to fluid flow. For long puddles and high wheelspeeds the governing equations decouple, leaving a Stefan problem for the shape of the solidification front and temperature fields. This problem has an analytic solution. The linear front corresponding to thin ribbons is a limiting case. Nonequilibrium kinetics at the freeze interface and undercooling of the melt are included in the general solution. These influences on solidification are thereby examined. Results are compared to previous solidification models and experiments.

1. INTRODUCTION

The planar-flow spin-casting process produces a continuous ribbon of microcrystalline or amorphous material. The liquid metal is directed onto a spinning wheel by a nozzle which is placed so close to the wheel that it interferes with the puddle of molten metal. The small gap between nozzle and wheel enhances overall process stability and delivers wider ribbons than otherwise possible, as is well-known. In a typical planar-flow setup (Fig. 1(a)), the hot nozzle (700°C, for aluminum) is held fixed above the spinning cold wheel (30°C, say) which moves with a linear velocity of about 10 m s^{-1}. The physics of planar-flow casting involves large thermal and velocity gradients as well as impact under pressure and phase-change.

The flow of metal is driven by the pressure applied to the molten metal reservoir. Solidification takes place if sufficient heat is extracted to (i) cool the superheated molten metal to or below its melt temperature and to (ii) remove the latent heat from the solidification front. The heat flows from the liquid to the chill-wheel heat sink. Heat transfer resistance due to conduction through the solidified material and resistance due to imperfect thermal contact with the wheel are the two relevant resistances. After solidification has begun, the heat must be extracted through the already solidified material.

Planar-flow casting is directional solidification [1]. The pulling is transverse, though, since solidified product is spun from the zone of solidification. The zone can be long and thin with a solidification front 100 times as long as the final ribbon thickness. Both these features distinguish planar-flow from conventional directional solidification. The long thin puddle means that the solidification front is of small slope, on average, with the consequence that average solidification rates can be much slower than the linear wheelspeed. Furthermore, the geometry forces the fluid flow to be orthogonal to the heat flux on average and this results in weak coupling between the fluid mechanics and heat transfer. This key feature is the basis for our analysis.

The process is "successful" if a continuous uniform ribbon emerges, all the solidification having taken place during contact with the wheel. The process can fail in a variety of ways, described elsewhere [2]. For a successful run the solidification rate must be compatible with the feed rate of molten metal. Heat transfer controls the shape of the solidification front while the fluid mechanics limits the ribbon thickness.

Casting can be successful under a variety of conditions. Our analysis is motivated by the conditions appropriate to our experiments [2]. In particular, the slow solidification rate relative to wheelspeed does not favor amorphous microstructures (working material permitting). Nevertheless, solidification rates can reach the limit of absolute stability for some alloys (e.g. 10 cm s^{-1}). Our interest is in the process behavior, however. For that reason, in our experiments we have

† Author to whom correspondence should be addressed.

NOMENCLATURE

c, A, D constants
B_s, $B_l \equiv H_w G/k_s$, $H_w G/k_l$ Biot number: solid, liquid
$B_{s0} \equiv k_{ls}(1-\Delta T_m)/\Delta T_m$ parameter (threshold Biot)
$C \equiv \mu U/2\sigma$ capillary number
C_{ps}, C_{pl} specific heats: solid, liquid
$\mathbf{e}_x$ unit vector, streamwise direction
E nozzle slot extent, cross-stream
$-f\lambda k_i$ attachment rate
g nonequilibrium interface function
h, h_∞ height of solidification front, far downstream
G nozzle/wheel gap
H mean curvature
H_w heat-transfer coefficient (wheel)
k_s, k_l, k_{ls} thermal conductivity: solid, liquid, ratio
L puddle length
$m(x, y, t)$ meniscus shape
$\mathbf{n}$ unit normal vector
p, p^* pressure: scaled, dimensional
P_s, $P_l \equiv \rho_s C_{ps} UG/k_s$, $\rho_l C_{pl} UG/k_l$ Peclet number: solid, liquid
Q volumetric flowrate
q_s heat flux in solidified material
$\mathbf{q}$, $\mathbf{q}_s$, $\mathbf{q}_l$ heat flux vector, in solid and liquid
R nozzle slot breadth
R_g ideal gas constant
s, s^* arclength, total
$\mathbf{t}$ traction vector
T, T^* temperatures: scaled, dimensional
T_i, T_i^* interface: scaled, dimensional
T_s, T_l solid, liquid regions
T_c, T_h, T_m constants, cold, hot, melting
u, u^* streamwise velocity: scaled, dimensional
U wheel speed
v, v^* vertical velocity: scaled, dimensional
V local solidification rate
$\bar{V}$ average solidification rate
$V^* \equiv k_s(T_h - T_c)/\rho_s \Delta\eta G$ a solidification rate (estimate)
$V^{**} \equiv [(-f\lambda k_i)\Delta s/R_g](T_m - T_c)/T_m$ attachment velocity
$W \equiv \rho_l U^2 G/2\sigma$ Weber number
x, x^* streamwise coordinate: scaled, unscaled vertical coordinate: scaled, unscaled.

Greek symbols
$\Delta\eta$ enthalpy of formation
Δp pressure drop, unscaled
$\Delta P \equiv \Delta p/\rho_l U^2$ applied pressure
ΔS entropy of formation
$\Delta T_m \equiv (T_m - T_c)/(T_h - T_c)$ quench fraction
$\varepsilon \equiv V^*/U$ solidification parameter
Γ liquid/solid interfacial energy
$\kappa \equiv V^*/V^{**}$ attachment parameter
$\bar{\kappa} \equiv [\Delta T_m/(1-\Delta T_m)]\kappa$ scaled attachment parameter
μ viscosity
ρ, ρ_s, ρ_l density, solid and liquid
σ surface tension
θ scaled temperature
τ^* ribbon thickness, dimensional
$\tau = \tau^*/G$ ribbon thickness, scaled.

not varied the working material. Only nominally pure aluminum and closely related alloys have been used. Tables 1 and 2 are based on these experiments. For the experiments, the relatively poor thermal contact with the wheel implies that undercooling is negligible. Nucleation rates are also much higher than solidification rates and therefore equilibrium prevails at the interface. Below, for completeness, however, we have included nucleation kinetics in the formulation. The analytical solution of the Stefan problem illustrates its influence.

Many previous models of spin-casting have pertained to the chill-block configuration. Davies modeled the chill-block process using a two-dimensional boundary-layer equation coupled with a boundary-layer type heat transfer equation [3]. Heat of solidification was not included in the analysis and the layer of solid metal was assumed to be the thickness of the boundary layer. Gutierrez and Szekely [4] modelled the planar-flow method in a similar manner but included the heat of solidification. Using a lubrication equation to model the fluid flow, they solved a heat balance which included convection in the direction of the spinning wheel and conduction normal to the wheel surface. Analyses by Takeshita and Shigu [5], Clyne [6], and Chu *et al.* [7] are the first melt-spinning models to include nonequilibrium solidification kinetics. These three use transient, pure conduction energy equations to model the heat transfer in each phase; they circumvent solving the momentum equation by assuming a plug flow velocity in the melt. Usually, the heat flux along the upper surface of the molten puddle is assumed zero (more appropriate for chill-block casting, as previously discussed [8]). More recent numerical models also make such assumptions (e.g. Ludwig *et al.* [9], Wang and Matthys [10]). In all

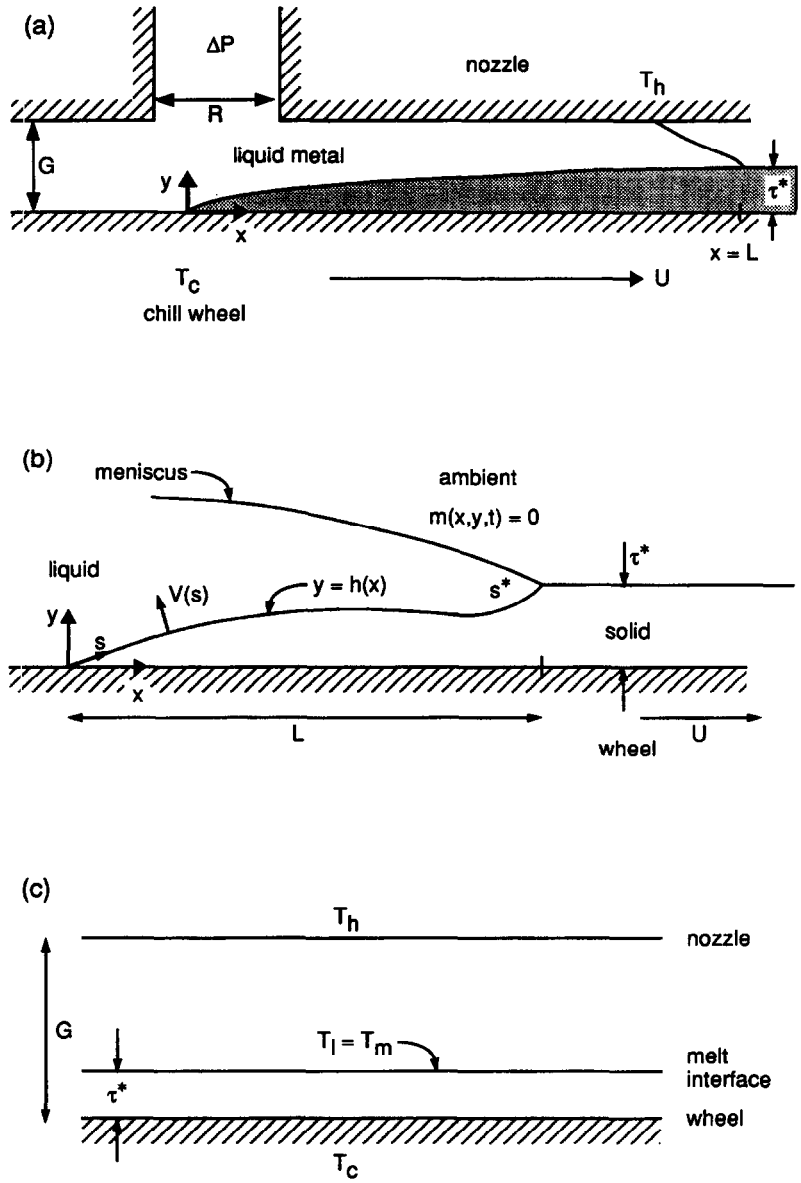

Fig. 1. Definition sketches for: (a) the puddle region; (b) steady-state solidification kinematics; (c) heat transfer through the solidified material for small slope and long puddle.

of these analyses the equations were solved numerically. Wang and Matthys [11] have estimated undercooling in the planar-flow process using their numerical method.

Solutions are obtained below to the steady-state continuity, momentum and energy equations in liquid and solid regions. The asymptotic limit is taken with respect to two small parameters. The ratio of solidification rate to wheelspeed, the "solidification" parameter, controls the slope of the solidification front and the ratio of puddle length to height, the "puddle" parameter controls the geometry of the flow domain. The size of other dimensionless parameters relative to the solidification parameter is guided by experiment (Tables 1 and 2).

The paper is organized as follows. Salient features of the process are described in the next section. Then, the solidification parameter is defined and shown to control the average slope of the front based on solidification kinematics. The governing equations are formulated and scaled. That the decoupling of the heat transfer and fluid mechanics follows from the small slope and long puddle assumptions is then demonstrated. Properties of the resulting Stefan problem are noted and an analytic solution is obtained. That solution does not require knowing the position on the

Table 1. Process parameters with typical values

Nozzle geometry		
G	10^{-3} m	nozzle/wheel gap
R	3×10^{-3} m	nozzle slot breadth
E	5×10^{-2} m	nozzle slot extent.
Process variables		
τ^*	10^{-4} m	ribbon thickness
U	10 m s^{-1}	wheel speed (linear)
Δp	5×10^{3} N m^{-2}	pressure drop
T_h	1033 K	superheat temperature
T_c	298 K	quench temperature.
Material properties (aluminum unless otherwise noted)		
ρ_s, ρ_l	2.7×10^{3}, 2.3×10^{3} kg m^{-3}	solid, liquid density
k_s, k_l	229, 103 J m^{-1} s^{-1} K^{-1}	solid, liquid thermal conductivity
C_{ps}, C_{pl}	938, 1080 J kg^{-1} K^{-1}	solid, liquid specific heats
μ	10^{-3} kg m^{-1} s^{-1}	viscosity (1033 K)
σ	0.86 N m^{-1}	surface tension (1033 K)
T_m	933 K	melting temperature
$\Delta\eta$	3.87×10^{5} J kg^{-1}	enthalpy of formation (933 K)
Γ	1.08 J m^{-2}	liquid/solid interfacial energy density (933 K)
$-f\lambda k_i$	30.8 m s^{-1}	attachment rate
H_w	1.1×10^{5} W m^{-2} K^{-1}	heat-transfer coefficient (solid/liquid contact with wheel).
Derived quantities (dependent parameters)		
$V^* \equiv k_s(T_h-T_c)/\rho_s\Delta\eta G$	0.16 m s^{-1}	a solidification rate
$V^{**} \equiv [(-f\lambda k_i)\Delta S/R_g](T_m-T_c)/T_m$	29 m s^{-1}	an attachment rate.

Table 2. Dimensionless groups with typical values

Geometry		
R/G	3	slot breadth
E/G	50	slot extent
Process		
$\tau \equiv \tau^*/G$	10^{-1}	ribbon thickness
$\Delta P \equiv \Delta pG/2\sigma$	3	applied pressure
$W = \rho_l U^2 G/2\sigma$	10^{2}	Weber number
$C \equiv \mu U/2\sigma$	10^{-2}	capillary number
$\varepsilon \equiv V^*/U$	10^{-2}	solidification parameter
P_s, $P_l \equiv \rho_s C_{ps} UG/k_s$, $\rho_l C_{pl} UG/k_l$	10^{2}, 10^{2}	Peclet number (solid, liquid)
$(T_h-T_m)/(T_h-T_c)$	0.14	superheat fraction
$\Delta T_m \equiv (T_m-T_c)/(T_h-T_c)$	0.86	quench fraction
Material		
B_s, $B_l \equiv H_w G/k_s$, $H_w G/k_l$	0.48, 1.1	Biot number (solid, liquid)
ρ_l/ρ_s	0.85	contraction ratio
k_l/k_s	0.45	conductivity ratio
$\Gamma T_m/(G\rho_s\Delta\eta)(T_h-T_c)$	10^{-6}	interfacial energy parameter
$\kappa = V^*/V^{**}$	0.0034	attachment parameter

wheel where solidification starts. This issue of initial solidification is then discussed on the basis of the solution to an auxiliary problem. Finally, the results are discussed relative to the literature.

2. PROCESS OVERVIEW

Parameters, dimensionless groups and assumptions

The term "planar-flow" refers to the narrow channel between the stationary nozzle face and the spinning wheel shown in schematic in Fig. 1(a). For typical wheel diameters (1 m, say), the wheel curvature is negligible in the gap and the boundaries are indeed "planar", although not necessarily parallel. The molten metal puddle is held between the hot nozzle face and cold chill wheel by surface tension. A ribbon of solidified metal is drawn out from beneath the puddle by the spinning wheel.

Typical values for the geometry, process variables and material properties (aluminum) are listed in Table 1. Given a particular experiment, all parameter values are available to a precision, as indicated, except the heat-transfer coefficient which is difficult to measure directly, as is well-known [e.g. 12]. We have measured it for our apparatus using data from thermocouples embedded in the wheel, in conjunction with an inverse

solution of the heat equation, to obtain $H_w = 1.1 * 10^5$ W m^{-2} K^{-1} [13]. An independent method, described below under Discussion, applied to the same apparatus gives $H_W = 1.7 * 10^5$ W m^{-2}–K^{-1} [14, 15]. In view of the resolution of data from experiments, it is adequate to use a contact-averaged coefficient, even though it is well-accepted that the coefficient varies with position [16]. The value in Table 1 comes from ref. [13]. The heat-transfer coefficient will enter the analysis through only one dimensionless group (Biot number) so that its uncertainty can be isolated. Values of the control parameters are from our experiments [2].

Table 1 also lists two dependent parameters. Important for the present discussion is V^*, a solidification rate. The other, V^{**}, is an attachment rate that arises from a kinetic expression commonly used for pure metals [17]. The definition of V^* is motivated as follows. The process is "successful" if all the molten metal forced through the nozzle solidifies before leaving the wheel. The heat of solidification (at least) must be fully absorbed by the wheel in that case. The heat-flux balance across the solidification interface (unit normal $\mathbf{n}$) is

$$(\mathbf{q}_s - \mathbf{q}_l) \cdot \mathbf{n} = \rho_s \Delta\eta V \tag{1}$$

where $\mathbf{q}_s$ and $\mathbf{q}_l$ are the heat fluxes in the solid and liquid, respectively, and V is the local solidification rate. Neglecting $\mathbf{q}_l$ and using typical values for $\mathbf{q}_s$ we estimate V using only parameters that can be measured or controlled (i.e. replace V by V^*, etc.). This estimate serves to define a typical solidification rate V^* (Table 1).

A small V^* relative to the wheel speed U decouples the heat and fluid flow, as will be shown. The solidification parameter is defined as,

$$\varepsilon \equiv V^*/U. \tag{2}$$

It controls solidification directly as shown in the next section. Table 2 lists a set of dimensionless groups, including ε, which are formed from the parameters in Table 1. The complexity of the process is apparent even with the reduction from 21 independent parameters (Table 1) to 17 dimensionless groups (Table 2), as dictated by dimensional analysis.

The relative importance of various effects is seen in Table 2. The applied pressure Δp is limited by the surface tension σ which holds the molten metal in the puddle. Inertia is typically much larger than surface tension which, in turn, is much larger than viscous forces (c.f. Weber and capillary numbers). This ordering distinguishes melt spinning flows from coating flows [18, 19]. In particular, inertia forces are four orders of magnitude larger than viscous forces within the bulk flow. Such a Reynolds number (recall, Reynolds = WC^{-1}) does not necessarily indicate turbulent flow, however [20]. The appropriate velocity scale is based on mass flux. It gives a Reynolds number of 10^3. Moreover, the solidification front is a sink of mass that tends to stabilize flow disturbances. The flow is assumed laminar.

The long extent of the slot in cross-stream direction E/G justifies a two-dimensional analysis (Table 2). The small superheat fraction $(1 - \Delta T_m)$ allows average values for the material properties of the melt to be used. In addition, since the material properties of the solid are relatively insensitive to temperature variations, both liquid and solid properties are taken to be constants. A closer look shows that even if temperature changes within the liquid layer are as large as 200 K and changes within the solid, 500 K, the change in viscosity and heat capacity is on the order of 25%, the change in thermal conductivity less than 15%, and the changes in density and surface tension are each less than 5% (based on data collected by Hatch [21]). The values used in the model should be viewed as averages across appropriate regions.

Solidification kinematics

The constraints imposed by the heat and mass balances must be compatible. Consider the kinematics of solidification. Figure 1(b) shows an arbitrary solidification front described by a smooth curve, $y = h(x)$. For a solidification interface, steady in the laboratory frame, kinematics give a local speed of solidification V (rate of propagation of interface normal to itself),

$$V(x) = U \frac{h'}{(1 + (h')^2)^{1/2}} \tag{3}$$

where primes denote derivatives with respect to x. The average rate of solidification is defined with respect to arclength s along the interface measured from the first point of solidification,

$$\bar{V}(s) = \frac{1}{s} \int_0^s V \, ds. \tag{4}$$

These kinematics allow for remelting ($h' < 0$) as well as solidification ($h' > 0$).

The total flux (volumetric) of material solidified along the front is

$$Q \equiv \int_0^{s^*} V \, ds = s^* \bar{V}(s^*) \tag{5}$$

where s^* is the arclength of interface at which the last bit of liquid solidifies (Fig. 1(b)). Position s^* corresponds to the intersection of the meniscus with the solidification front and is a three-phase common point. Here, the ribbon reaches its final thickness $\tau^* = h(L)$ and, for successful production, the ribbon is still in contact with the wheel at $x = L$. A straightforward evaluation of the integral in eqn (5) using expression (3) verifies that,

$$s^* \bar{V} = \tau^* U, \tag{6}$$

equivalent to a mass balance for the system.

Equation (6) relates the heat transfer via $\bar{V}$ to the

mass flow. For $\bar{V}/U$ sufficiently small, the length of the solidification front s^* approaches L (barring "fractal" interfaces) and hence eqn (6) reduces to (cf. Fig. 1(b)),

$$\tau^* U = L\bar{V} \quad \text{as} \quad \bar{V}/U \to 0. \tag{7}$$

This key relationship shows that the average slope of the front is small for high wheelspeeds,

$$\tau^*/L = \bar{V}/U \quad \text{as} \quad \bar{V}/U \to 0. \tag{8}$$

The long thin domain (aspect ratio τ^*/L) is controlled by high wheelspeed and is consistent with a long puddle.

The average solidification rate $\bar{V}$ and the typical solidification rate V^* are not necessarily equal. For high wheelspeeds (i.e. $\bar{V}/U \to 0$), they differ by an order one constant, as we show now. An explicit expression for this constant results from the solution presented below.

The high wheelspeed limit $\bar{V}/U \to 0$ is equivalent to $\varepsilon \equiv V^*/U \to 0$. This can be seen from eqn (1), neglecting any heat flux through the liquid and using eqn (3),

$$q_s \sim \rho_s \Delta\eta U\tau^*/L = k_s(T_h - T_c)/G(U/V^*)(\tau^*/L), \tag{9}$$

where the definition of V^* has been used for the right most expression. Requiring q_s to be order one, relation (9), shows that

$$\tau^*/L \sim \varepsilon \quad \text{as} \quad \varepsilon \to 0. \tag{10}$$

Hence, V^* is proportional to $\bar{V}$ (cf. eqn (8)) and the average slope of the front is controlled by the solidification parameter ε as $\varepsilon \to 0$.

3. PROBLEM FORMULATION

The puddle region extends vertically from the wheel surface below to the nozzle face above and horizontally from the upstream meniscus to downstream where all metal has been solidified (Fig. 1). This is the problem domain. The governing equations are energy and momentum equations in the bulk (liquid and solid) along with the energy and momentum boundary conditions at the solidification front (internal boundary) and at the external domain boundaries. The position and shape of several boundaries are part of the solution. The upstream and downstream menisci and the melt interface are all undetermined beforehand. The ends of these surfaces are points of two and three-phase moving contact. Classical boundary conditions are assumed for these since, once casting is successful, details of contact-line behavior appear not to dominate the behavior. The bulk equations, conditions at the solidification interface and the boundary conditions are listed in Table 3. The function g that appears in the interface condition allows for Gibbs–Thomson and nonequilibrium kinetics ($g \neq 1$). Specific contributions to g are an interfacial energy and a correction for finite attachment kinetics, as evident from the nondimensional version of the condition (interfacial temperature, Table 4). The correction is a linearization about the melt temperature of the more general expression, appropriate for small to moderate undercooling [6].

Table 3. Governing equations and boundary conditions (T^* has been replaced by T for clarity in this table)

Equations	
Solid region	
$\rho_s C_{ps} U(\partial T_s/\partial x) = k_s \nabla^2 T_s$	(energy balance).
Liquid region	
$\nabla \cdot \mathbf{u} = 0$	(continuity)
$\rho_l \mathbf{u} \cdot \nabla \mathbf{u} = -\nabla p + \mu \nabla^2 \mathbf{u}$	(momentum balance)
$\rho_l C_{pl} \mathbf{u} \cdot \nabla T_l = k \nabla^2 T_l$	(energy balance).
Solidification front	
$\mathbf{n} \cdot (k_s \nabla T_s - k_l \nabla T_l) = \rho_s \Delta\eta V$	(energy balance).
Boundary conditions	
Heat transfer boundary conditions	
$T = T_h$	(nozzle face)
$T = T_m g\{V, V^{**}, \Gamma\}$	(solidification front)
$\mathbf{q} \cdot \mathbf{n} = H_w(T - T_c)$	(chill wheel)
$\mathbf{q} \cdot \mathbf{n} = 0$	(liquid/air meniscus).
Fluid mechanics boundary conditions	
$\mathbf{u} = \mathbf{0}$	(nozzle face)
$\mathbf{u} = U\mathbf{e}_x$	(solidification front)
$[\mathbf{t}] = (2\sigma H)\mathbf{n}$	(liquid/air meniscus)
$\mathbf{u} \cdot \nabla m = 0$	(liquid/air meniscus, kinematic).

The system of equations is complicated. Numerical solution for general parameter values is one approach, an approach that can challenge numerical techniques. Our approach, a complementary one, uses asymptotic analysis based on the separation of scales. This parameter regime of relevance is a restricted one, yet one of technological interest.

Material properties are taken to be constant, as discussed above. Two thermal influences on momentum transfer that have been neglected in the governing system (Table 3) deserve special mention, however. First, the momentum equation in the bulk liquid has no buoyancy term. This is justified since the system is stably stratified on average (heated from above) and since the region of interest is long and thin. Second, the jump in traction vector $\mathbf{t}$ at the upstream and downstream menisci has only a normal component; hence any influence due to surface-tension gradients (Marangoni stresses) has been neglected. An estimate of net thermocapillary shear force for a clean interface as compared to net viscous shear force justifies this approximation. Moreover, the interface is likely to be

Table 4. Scaled equations and boundary conditions

Equations

Solid region

$$P_s\left(\frac{G}{L}\right)\frac{\partial T_s}{\partial x}=\left(\frac{G}{L}\right)^2\frac{\partial^2 T_s}{\partial x^2}+\frac{\partial^2 T_s}{\partial y^2} \quad \text{(energy balance).}$$

Liquid region

$$\frac{\partial u}{\partial x}+\frac{\partial v}{\partial y}=0 \quad \text{(continuity equation)}$$

$$W\left(u\frac{\partial u}{\partial x}+v\frac{\partial u}{\partial y}\right)=-\frac{\partial p}{\partial x}+C\left(\frac{L}{G}\right)\left[\left(\frac{G}{L}\right)^2\frac{\partial^2 u}{\partial x^2}+\frac{\partial^2 u}{\partial y^2}\right] \quad \text{(momentum balance)}$$

$$W\left(\frac{G}{L}\right)\left(u\frac{\partial v}{\partial x}+v\frac{\partial v}{\partial y}\right)=-\frac{\partial p}{\partial y}+C\left(\frac{G}{L}\right)\left[\left(\frac{G}{L}\right)^2\frac{\partial^2 v}{\partial x^2}+\frac{\partial^2 v}{\partial y^2}\right]$$

$$P_l\left(\frac{G}{L}\right)\left(u\frac{\partial T_l}{\partial x}+v\frac{\partial T_l}{\partial y}\right)=\left(\frac{G}{L}\right)^2\frac{\partial^2 T_l}{\partial x^2}+\frac{\partial^2 T_l}{\partial y^2} \quad \text{(energy balance).}$$

Solidification front

$$-\varepsilon k_{ls}\left\{-\left(\frac{G}{L}\right)^2\left(\frac{dh}{dx}\right)\frac{\partial T_l}{\partial x}+\frac{\partial T_l}{\partial y}\right\}=\left(\frac{G}{L}\right)\left(\frac{dh}{dx}\right) \quad \text{(energy balance)}$$

$$-\varepsilon\left\{-\left(\frac{G}{L}\right)^2\left(\frac{dh}{dx}\right)\frac{\partial T_s}{\partial x}+\frac{\partial T_s}{\partial y}\right\}$$

$$T_i=\Delta T_m\left\{1-\left(\frac{U}{V^*}\right)\left(\frac{G}{L}\right)\kappa\frac{dh}{dx}\Big/\left[1+\left(\frac{G}{L}\right)^2\left(\frac{dh}{dx}\right)^2\right]^{1/2}\right\} \quad \text{(interface temperature)}$$

$$+(\Gamma T_m/\rho_s\Delta\eta G(T_h-T_c))\left(\frac{G}{L}\right)^2 2H$$

where $2H\equiv\dfrac{d^2h}{dx^2}\Big/\left(1+\left(\dfrac{G}{L}\right)^2\left(\dfrac{dh}{dx}\right)^2\right)^{3/2}$.

Boundary conditions

Heat transfer boundary conditions

$T_l=1$ at $y=1$ (nozzle face)

$T_l=T_s=T_i$ (solidification front)

$0=B_sT_s-\dfrac{\partial T_s}{\partial y}$ at $y=0$ (chill wheel)

oxidized (for aluminum in air), further reducing such effects.

Decoupling of momentum and heat transfer

The temperature and velocity fields governed by the equations of Table 3 are coupled. The modes of coupling are (i) advection of energy in both the liquid and the solid regions and (ii) the position and shape of the solidification front which defines the flow domain. It is now shown how coupling (i) is broken for high wheelspeeds and that, consequently, the heat transfer and fluid mechanics problems decouple.

Scales are introduced into the governing equations motivated by Tables 1 and 2. Starred and unstarred quantities represent dimensional and scaled variables, respectively.

$$x^*=Lx,\quad y^*=Gy \quad \text{lengths}$$

$$u^*=Uu,\quad v^*=u(G/L)v \quad \text{velocities}$$

$$p^*=(2\sigma/G)p \quad \text{pressure}$$

$$T^*-T_c=(T_h-T_c)T \quad \text{temperature.}$$

The momentum x-length scale is assumed the same as the heat transfer x-length scale. The vertical velocity scale is implied by the horizontal scale through the continuity equation in the standard way. The pressure scales on the surface tension "blow-out" pressure, the

largest pressure sustainable by a static meniscus of curvature $(2/G)$. The temperature scales by the maximum temperature difference across the gap. Substituting this change of variables leads to the governing system listed in Table 4 (dimensionless).

The strength of advection in the liquid and solid regions is represented by the $(G/L)P_l$ and $(G/L)P_s$ coefficients, respectively. Advection is suppressed by long puddles. We have used high-speed cinematography to directly observe the puddle region. Measurements of puddle length are typically $L \approx 20$ G [14, 15]. This is consistent with Wilde and Matthys [22] who report $L \approx 10$ G despite a restriction on maximum L due to their crucible construction. These observations motivate a 'long-puddle' limit. It is assumed that,

$$\tau^*/L \to 0 \quad \text{small slope}$$

and

$$G/L \to 0, \quad \text{long puddle}$$

for

$$\varepsilon \to 0, \quad \text{high wheelspeed.}$$

For Peclet numbers of order one, the advection terms in the governing system are negligible in the above limit and the temperature field uncouples from the velocity field. The temperature field still influences the fluid mechanics by determining the flow domain (the shape of the solidification front). The strategy is to solve first for the temperature fields in the liquid and solid to find the shape of the solidification front. The latter fixes the boundary of the fluid flow problem which can be solved then for the velocity field. Corrections that account for weak coupling may be found by the perturbation approach. The solution of the thermal/solidification problem obtained below is the lowest order solution in the perturbation hierarchy. The solution of the fluid flow problem has been outlined [23] and details appear elsewhere [24]. See Steen and Karcher [25] for a review of the fluid mechanics of spin-casting.

For typical melt-spinning operations, do temperature and velocity fields actually uncouple? Straightforward evaluation using $G/L \approx 0.05$ and the values of Table 1 yields $(G/L)Pe_s \approx 5$ and $(G/L)Pe_l \approx 10$. At first sight, then, uncoupling seems invalid. On the other hand, recall that these measures of coupling depend on the velocity and length scales chosen. For example, the vertical scale G was chosen for both liquid and solid regions, for simplicity. But the solid layer is much thinner, order T/G thinner, than the liquid layer. Hence, a more accurate measure of advective coupling in the solid is actually $(T/G)^2$ less than cited; that is, about 0.05 (c.f. Table 4). In a similar way, a more appropriate velocity scale for the liquid region is based on mass flow rate, i.e. $(T/G)U$. Using such a scale reduces the cited coupling from order ten to order one. Hence, uncoupling in the liquid is only borderline inappropriate. Also relevant is the stability of flow in the gap. An unstable flow will tend to make L an inappropriate streamwise scale. Regardless of casting conditions in any particular laboratory, however, decoupling provides a valuable limiting case and a framework for understanding finite coupling.

The Stefan problem

Decoupling leads to a Stefan problem for the heat flow. Sufficient heat must be extracted to the chill wheel for solidification to occur. If recalescence is to occur, significant heat transfer to the wheel is required to undercool the melt initially. Suppression of nucleation within the melt determines the extent of undercooling. Measurements and/or estimates of this effect are difficult. In modeling, undercooling is usually an input parameter. Planar-flow casting is a rather "dirty" system and abundant heterogeneous nucleation is likely. Even if significant undercooling were to occur, consequent recalescence would be a local effect, confined to a neighborhood of first contact of the melt with the wheel. Initial solidification is discussed in detail in Section 5. For long puddles, undercooling is expected to have little effect on the average solidification behavior. Undercooling and recalescence are therefore neglected in this section.

The Stefan problem can be solved generally. A 1 D heat flux (vertical) is driven by the temperature drop and limited by a series of resistances. Conduction is dominant in the liquid and solid, coupled in series to the contact resistance which, in turn, is coupled to the conduction into the substrate. Interface shape enters through the latent heat source that depends on slope. The governing equations obtained are the steady heat equation in the solid $(0 < y^* < h)$ and liquid $(h < y^* < G)$ regions,

$$\mathrm{d}^2T^*/\mathrm{d}y^{*2} = 0 \tag{11a}$$

with boundary conditions,

$$k_s\,\mathrm{d}T^*/\mathrm{d}y^* = H_w(T^* - T_c) \quad \text{at} \quad y^* = 0, \tag{11b}$$

$$T^* = T_h \quad \text{at} \quad y^* = G, \tag{11c}$$

and the conditions at the front $(y^* = h(x))$

$$T^* = T_m \tag{11d}$$

$$q_s - q_l = -\rho_s \Delta\eta U\,\mathrm{d}h/\mathrm{d}x. \tag{11e}$$

Here we have restricted to $g = 1$, for simplicity, although the general solution reported later includes the effect of kinetics. Note that surface energy effects do not appear in the long puddle limit, in any case.

It is straightforward to reduce the Stefan problem (11) to an ordinary differential equation (ode) for the shape ($\bar{h} \equiv h/\tau^*$ in this nondimensional version, and drop overbars),

$$(c/\Delta T_m)\,dh/dx = B_s/(1+\tau h B_s) - B_{s0}/(1-\tau h) \quad (12a)$$

with

$$h(0) = 0 \quad \text{and} \quad h(1) = 1. \quad (12b)$$

Here,

$$B_{s0} \equiv k_{ls}(1-\Delta T_m)/\Delta T_m, \quad (13)$$

and c is the constant relating the average to characteristic solidification rate,

$$\bar{V} = cV^*. \quad (14)$$

The shape $h(x)$ and the parameters c and τ are unknown. The problem is under-determined; it yields a 1-parameter family of shapes. τ acts like a scaling factor. Physically, τ is determined by the solution of the fluid flow problem and, in particular, by the mass balance which limits the extent of the front. That solution is beyond the scope of this paper, however.

Several properties of this equation are noteworthy. Evaluating at $x = 0$, one sees that a physical solution (positive slope) requires

$$B_s > B_{s0}.$$

This is a restriction on the coefficient of heat-transfer to the wheel. If the contact resistance is too great, no solidification occurs.

The right-hand side of eqn (12a) is the difference of two positive terms, the first of which is decreasing and the second increasing with h. It follows that the front must be concave down, at least initially. Remelting can only occur if the right-hand side reaches zero, but such an h would be a stationary solution of the ode. By its first-order nature, it cannot reach such a state, at least at finite x. It follows that remelting cannot occur.

4. SOLUTION OF THE STEFAN PROBLEM

Differential eqn (12) can be solved analytically for any $0 < \tau < 1$. Nevertheless, it is instructive to first consider thin ribbons, $\tau \ll 1$, a particularly simple case. A linearization is then valid. The solution of the linearized version is immediate and yields c and, consequently,

$$\bar{V} = [B_s \Delta T_m - k_{ls}(1-\Delta T_m)]V^*. \quad (15)$$

This prediction can be used to relate processing conditions to microstructure. The right-hand side involves parameters that are controlled or known in principle, at least. For the values listed in Table 1, eqn (15) predicts an average rate, $\bar{V} = 5.6$ cm s^{-1}. Equation (15) can also be used to estimate B_s, and hence H_w, given $\bar{V}$. In this connection, direct measurement of $\bar{V}$ has been shown feasible by using a two-layer casting setup (Chu *et al.* [7]).

We consider the solution of the analog of ode (12) that includes kinetic effects ($\kappa \neq 0$). This ode is straightforward to obtain from Table 4 as the full decoupled Stefan problem (we shall not write it down). Note that, in eqn (12), h can be redefined to eliminate τ from the right-hand side ($\bar{h} \equiv h/G = h\tau$). If the right-hand boundary condition is abandoned, one is left with an initial-value-problem depending on a single scaling parameter that controls the initial slope. Stated differently, the solidification shape is determined up to a constant, to be fixed by an auxiliary condition. The same holds for the analog equation. Indeed, the constant c/τ can be absorbed in the x-coordinate (replace $\tau x/c$ by x). Using $\bar{h} \equiv h/G$ here, the general solution is given implicitly by (dropping overbar),

$$\begin{aligned} xA^3 = {} & A^2h^2/2 + (AD - A^2)h + \bar{\kappa}A^2(1-A)h \\ & + A^2h/B_s + [D^2 - AD(1-\bar{\kappa}) \\ & + (AD - A^2(1+B_s\bar{\kappa}))/B_s]\log(1 - Ah/D) \end{aligned} \quad (16)$$

where

$$A \equiv \Delta T_m + k_{ls}(1-\Delta T_m)$$

$$D \equiv \Delta T_m - k_{ls}(1-\Delta T_m)/B_s,$$

and

$$\bar{\kappa} \equiv [\Delta T_m/(1-\Delta T_m)]\kappa.$$

The thickness τ is determined through the auxiliary condition $h(\tau/c) = \tau$. Knowing τ gives c, guaranteed by the monotonicity of h. Knowing c gives τ as a solution of a nonlinear transcendental equation. Again, monotonicity makes the solution unique. For $\kappa = 0$, eqn (16) yields the solution to eqn (12), as expected. Using (16), the isotherms in each of the phases may be determined by the relationships,

$$T_s(x,y) = \Delta T_m(B_s y + 1)[1 - \kappa\, dh/dx]/(B_s h + 1) \quad (17a)$$

$$T_l(x,y) = \{\Delta T_m(1-y)[1 - \kappa\, dh/dx] + (y-h)\}/(1-h). \quad (17b)$$

Equation (16) gives the asymptotic height in the limit as x approaches infinity, h_∞,

$$h_\infty = (\Delta T_m - k_{ls}(1-\Delta T_m)/B_s)/(\Delta T_m + k_{ls}(1-\Delta T_m)). \quad (18)$$

This height corresponds to the steady-state height of a one-dimensional, pure conduction problem solved with appropriate boundary conditions at infinity. Physically, one would expect this thickness, if there were no cut-off by the fluid flow. Two subcases are of interest. The thin ribbon limit $\tau \ll 1$ ($\kappa = 0$) can be recovered from eqn (16) by keeping just the linear terms in an expansion of the right-hand side. The case of perfect contact with the wheel ($B_s^{-1} = 0$) yields a solidification front where the quadratic term dominates, corresponding to "square-root" growth of the front.

A sample plot of solidification front and isotherms for parameters that exaggerate kinetic effects ($\kappa = 1$)

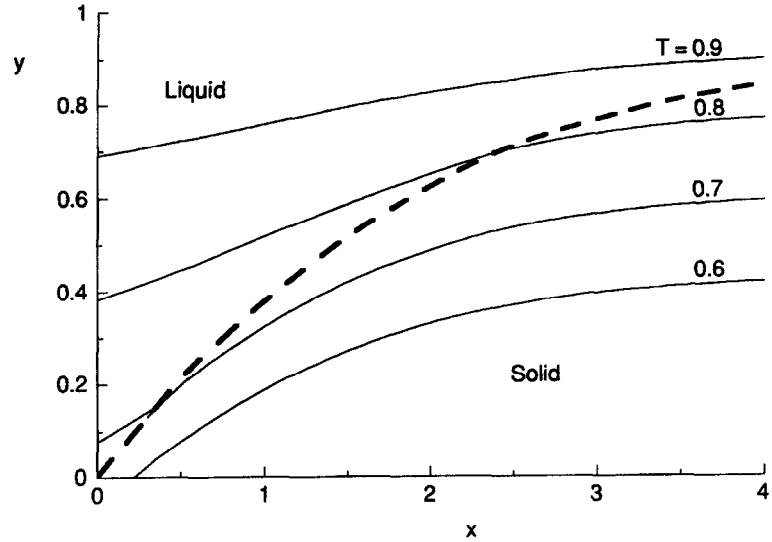

Fig. 2. Isotherms in puddle region according to analytic solution (eqn (17)) for strong interfacial kinetic effects, $\kappa = 1$ ($\Delta T_m = 0.86, k_{ls} = 0.45, B_s = 1.6$). Note difference in ordinate and abscissa scales.

is shown in Fig. 2 (other parameters as in Table 2). It must be emphasized that this is a demonstration of extreme kinetic effects. An appropriate κ for our casting of Al is two orders of magnitude smaller, in which case isotherms are nearly the shape of the solidification front, only translated one from another. Figure 2 shows the solidification front and isotherms in each phase. There is strong interfacial undercooling at the solidification front due to the solidification kinetics. Figure 3(a, b) shows the change in solidification front shape with changes in B_s and k_{ls}. For increases in B_s and decreases in k_{ls} the solidification front height is larger at fixed values of x. Figure 3(c) shows the change in final solidification thickness, h_∞, vs k_{ls} for different values of B_s. In this figure, h_∞ reaches zero when B_s is too small and/or k_{ls} too large for the metal to be cooled below its freezing point. This situation of unsuccessful ribbon production has been observed in experiment [2]. The amount of undercooling at the solidification front as a function of κ is shown in Fig. 3(d). The larger the value of κ, the more the undercooling. For $\kappa = 0$ the temperature of the solidification front is the equilibrium melting temperature. This case is the appropriate one to be compared to our experiments (see below).

5. INITIAL SOLIDIFICATION: AN AUXILIARY PROBLEM

The position on the wheel where solidification just begins is not determined by the above solution. Also, the shape of the front in a neighborhood adjacent to the initial solidification point is poorly approximated by the solution. Streamwise conduction and convection cannot be neglected there. We discuss both issues in this section. An auxiliary problem is solved to estimate an entrance length, the distance from first contact of the melt with the wheel to the point of first solidification.

The point of initial solidification in general depends on the nucleation kinetics and the temperature. Both can be influenced by the fluid flow. When non-equilibrium effects do not play a role, initial solidification is determined by where the molten metal is cooled to the melting temperature. Generally, however, the temperature field in the flow nearby can be useful in estimating the entrance length and the shape of the front near initial solidification, provided the solidified material does not substantially disturb the flow.

Consider the model problem of liquid heat transfer in a horizontally infinite layer without solidification and with boundary conditions as indicated in Fig. 4. A plug flow brings liquid at the hot temperature $\theta = 1$ into contact with a sudden change in lower boundary condition at $x = 0$, modeling the initial contact of the liquid with the wheel. The liquid cools from below and far downstream the temperature profile relaxes to a linear conduction profile. This problem includes convective effects and conduction parallel to the plates in addition to conduction normal to the plates. These assumptions make the governing energy equation a linear, second-order partial differential equation with constant coefficients, but because of the boundary conditions, an analytic solution is apparently not available. The governing equation and boundary conditions are nondimensionalized as follows,

$$x = x^*/G \quad y = y^*/G$$

$$u = u^*/U \quad v = v^*/U$$

$$\theta = (T^* - T_c)/(T_h - T_c).$$

The scaled system is solved numerically by a finite difference code.

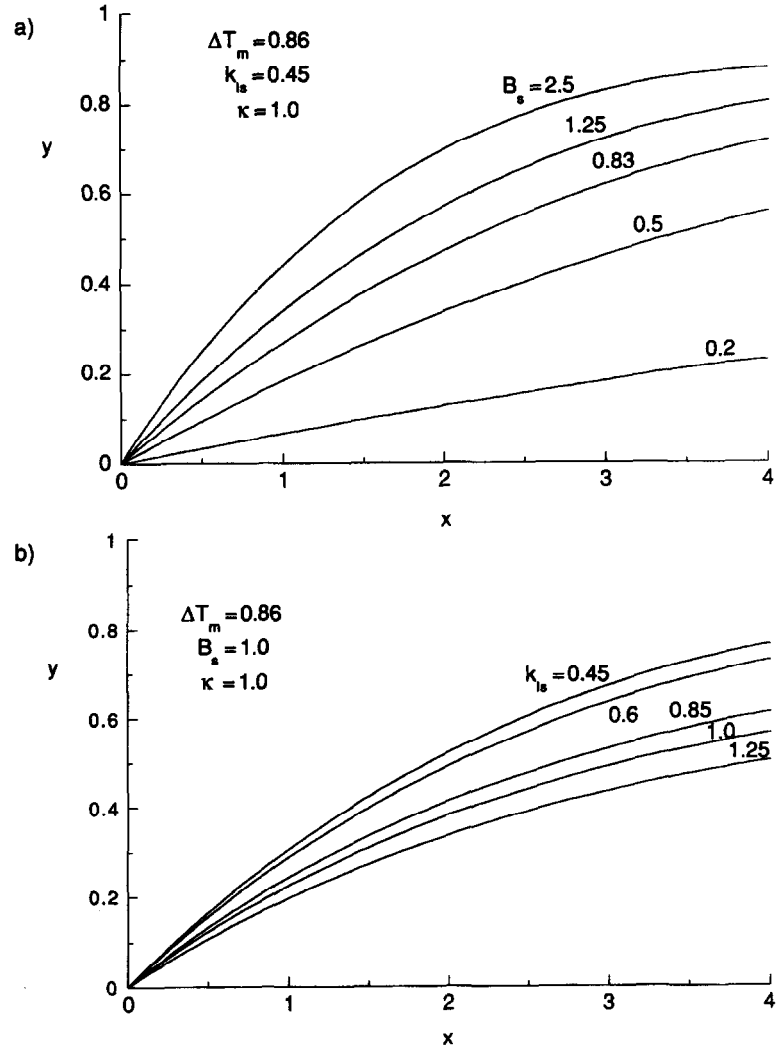

Fig. 3. (a) Shape of solidification front as it depends on Biot number B_s; (b) shape of solidification front as it depends on conductivity ratio k_{ls}; (c) asymptotic ribbon thickness h_∞ against conductivity ratio k_{ls} as it depends on Biot number B_s; (d) interfacial undercooling $T_m - T_i$ against attachment parameter κ. (*Continued overleaf.*)

A set of resulting isotherms for typical parameters (Table 1) is shown in Fig. 5. The entrance length is estimated by the number of gap sizes between the change in boundary condition and the point where the material starts to freeze. Here, assuming 100 K of undercooling, the entrance length is 2.4 gap lengths. This is a conservative estimate, likely to be an upper bound. To undercool a metal by 100 K without solidification, the material would have to be maintained particulate free to prevent heterogeneous nucleation [26, 27]. This is not the case in melt-spinning where the chill wheel typically provides many nucleation sites. As a check, the results of this numerical solution have been compared with two limiting cases of the general problem [24]. The analytical approximations give the same temperature profiles and the same order of magnitude for the entrance length.

The analysis of the liquid layer without solidification describes the temperature profiles qualitatively where the liquid starts to cool but before it begins to solidify. Typically, the length between the point where the metal starts to cool and where it starts to solidify is very short. Even for large undercooling in the process, we may expect the liquid to start solidifying very soon after contact with the wheel, perhaps within one gaplength or so, conservatively.

Sufficiently near the position of initial solidification the length scales for conduction in the x and y directions are comparable, no matter how strong convection is. Hence, there is some neighborhood where the long puddle assumption and therefore the high wheelspeed asymptotics must break down (cf. [6]). For the parameter regime of interest, however, this neighborhood is very small and has little effect on predictions of average solidification rate, puddle length and ribbon thickness. The utility of the solution of Section 4 remains. Mathematically speaking, we have obtained outer solutions in a singular pertur-

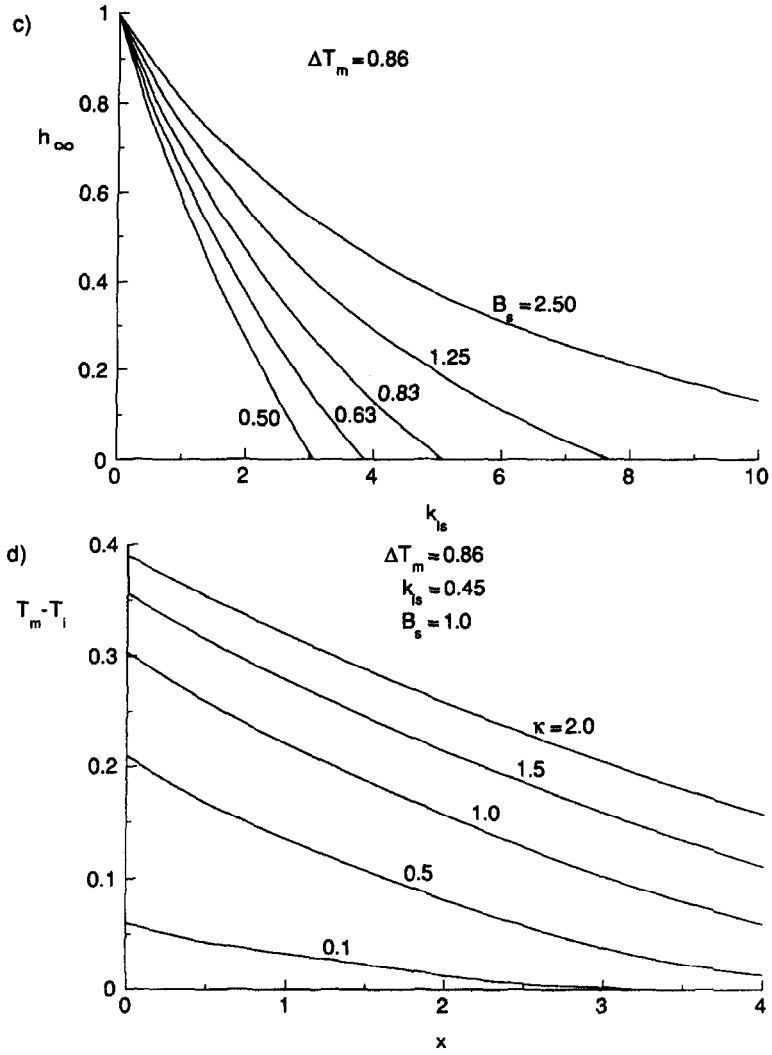

Fig. 3—*continued.*

bation problem. Details adjacent to the initial solidification point require resolving the boundary layer by solving the inner problem. That is, the curvature of the front and other interfacial effects are important in a narrow region that has not been resolved. A further justification for neglecting this region, at least as far as average quantities go, comes from previous work that has shown that nucleation kinetics have only a small effect on the overall time (i.e. length) needed for solidification [6, 7]. The interface velocity profiles calculated in the numerical solution of Wang and Matthys [11] clearly show a boundary layer structure although their formulation neglects streamwise conduction and interface curvature effects (precluding accurate representation of the physics near initial solidification).

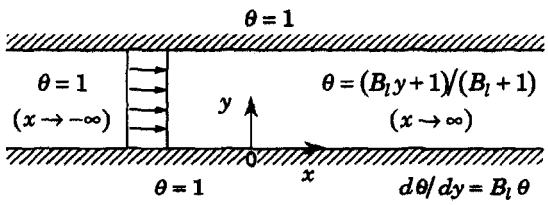

Fig. 4. Schematic of auxiliary problem (no solidification).

6. DISCUSSION

The solidification of a quiescent melt in contact with a constant temperature heat sink is a classical process metallurgy problem (e.g. [28]). The solidification front is a plane surface whose position is a function of time. Analysis shows that the height of the solidification front is proportional to the square root of time, provided the only resistance to heat flow is through the already-solidified metal (conduction-limited). In melt-spinning, the streamwise direction x plays the role of time t. In the extreme of infinite B_s, a Taylor series expansion of $h(x)$ for x near zero yields,

$$h \sim x^{1/2}.$$

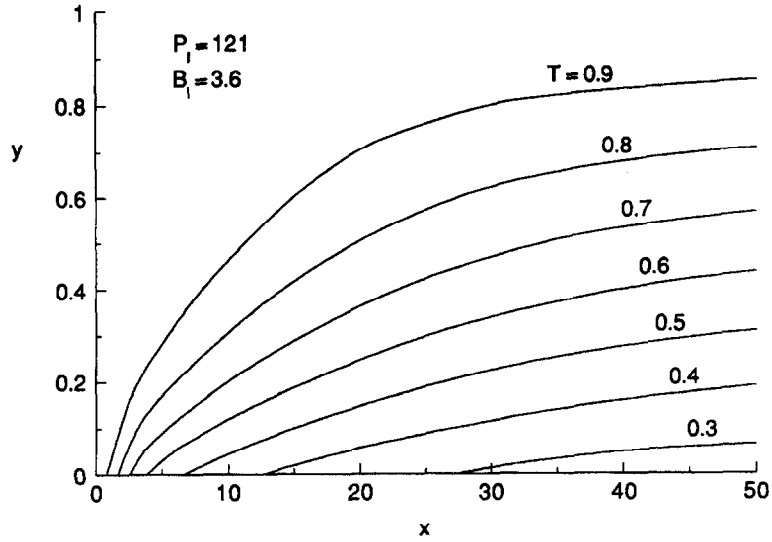

Fig. 5. Isotherms for auxiliary problem ($P_I = 121$, $B_I = 3.6$). Note difference in ordinate and abscissa scales.

Hence, conduction-limited growth is relevant to melt-spinning in the limit of good thermal contact or, equivalently, when x is small. In contrast, for a constant-flux lower boundary (contact-limited), the growth into a quiescent melt is linear [29]. One expects these cases to be the extremes of growth or, equivalently, the range of shapes of the solidification front.

In melt-spinning the solidification rate is not strongly affected by the boundary condition on the upper surface of the liquid puddle at the start of solidification, and in this limit similarly-shaped solidification fronts are found for both chill-block and planar-flow casting. Heat transfer analyses of the chill-block melt-spinning process by Kavesh [30] and Hillmann and Hilzinger [31] for an ideal heat sink show the same square root dependence for small x as in the quiescent melt problem. In addition, Hillmann and Hilzinger found in the Newton cooling regime (B_s finite) that the solidification height should depend linearly on x, and our solution predicts this same dependence for thin ribbons. In a qualitative solidification analysis, Jones [32] has determined maximum solidification front velocities for the melt-spinning process. Our solidification solution gives these same maximums at the point where solidification starts—where the heat transfer to the wheel is greatest—in the limit of no heat flux from the liquid phase (i.e. $k_{ls} \to 0$).

We measure growth in our experiments via direct measurement of L using high-speed cinematography. The residence time in the puddle of a liquid packet undergoing solidification is given by,

$$t_s \equiv L/U.$$

Thickness τ^* is measured by cutting and weighing ribbon sections. By doing a series of casts (different U), one obtains a set of data (t_s, τ^*). The growth curve is the plot of τ^* vs t_s and the growth exponent is obtained from the corresponding log–log plot [14]. A power law results,

$$\tau^* \approx 0.07 t_s^{0.84}.$$

It should be noted that the range of data is limited by the operability window of the process. For the prevailing conditions (Table 1), ribbons are typically thin ($\tau < 0.1$). The slope gives the velocity

$$\bar{V} \sim t_s^{-0.16}$$

which shows that growth is closer to linear ($t_s^{0.0}$) than to square root ($t_s^{0.5}$). The typical average solidification rate turns out to be ~ 5 cm s^{-1} from these measurements. This can be compared directly with the estimate of 5.6 cm s^{-1} for the linear front, eqn (15), noted above.

The growth curve can be used to back out H_w in conjunction with the model. The result is $H_w = 1.7 * 10^5$ W cm^{-2} K^{-1}. This should be compared to $H_w = 1.1 * 10^5$ W cm^{-2} K^{-1} obtained by an independent method as described above [13]. The agreement helps validate the solution of the Stefan problem. For thicker ribbons, we can compare with other work. For example, $\tau = 0.33$ with $B_s = 1$ gives a rate $V \approx 38$ cm s^{-1} (other parameters as in Table 2) from eqn (16). The numerical prediction of Wang and Matthys [11] for Al on an ideal wheel, $H_w = 1 * 10^6$ W m^{-2} K^{-1} ($B_s = 3.1$), is very close to this value. The average slope for the same metal but from a different apparatus is found by Chu *et al.* [7] to be 26 cm s^{-1}. A further comparison with Chu *et al.* [7] concerns their observation that the solidification rate in their experiments showed little or no change with wheel-speed. The solidification rate predicted by our solution is independent of the wheel speed, a consequence of the decoupling. Thus, a theoretical basis for their observation is provided.

Comparisons of temperature fields with previous work on chill-block casting must be qualitative since boundary conditions on the upper side of the liquid puddle differ. The analyses of Davies [3] and Gutierrez and Szekley [4] show the same general shape for the temperature profiles and solidification front along the length of the puddle. The temperature profiles across the nozzle wheel gap in the work by Clyne [6] and Chu *et al.* [7] show similar characteristics to the above solutions after the undercooling due to nucleation kinetics has recalesced. The recalescence usually takes place after only 10% of the layer is solidified. In these analyses, the temperature profiles across the gap are essentially pure conduction profiles in both the solid and liquid phases, with a small convective effect enhancing the temperature gradient in the liquid layer at the solidification front. Direct measurement of heat flux also shows a regime of constant flux for relative poor contacting [33].

7. CONCLUSIONS

Planar-flow melt-spinning is characterized by its long thin solidification zone. This forces the fluid flow to be orthogonal to the heat flux, on average, and is responsible for uncoupling the heat-transfer/solidification from the fluid mechanics. The long zone also implies a slow solidification rate (on average) relative to wheelspeed. Although absolute solidification rates can be high (rapid solidification), they are typically several orders of magnitude smaller than the wheelspeed, their upper limit. The thinness of the puddle zone suppresses convection. Heat transfer nevertheless influences the fluid flow by determining the flow domain.

The Stefan problem that results has noteworthy properties. A threshold heat-transfer coefficient, that depends on conductivities and relative temperature drops across liquid and solid, must be exceeded for solidification to start. Once solidification occurs, there is no remelting along the front. It has a positive but monotone decreasing slope.

The Stefan problem is solved analytically. Important limiting cases are the thin ribbon which has a linear front and the thick ribbon formed under perfect contact with the substrate which has a square-root dependence on position. These are the two limiting growth behaviours; all other cases fall between them. These two cases parallel the conduction-limited and contact-limited cases of uni-directional solidification into a quiescent melt. Our experiments show a growth that is closer to linear than square-root. The predictions are in agreement with the limited data.

Issues of nonequilibrium solidification kinetics and undercooling are discussed. The solution of the Stefan problem illustrates the influence of nonequilibrium effects and an auxiliary problem shows how undercooling can delay solidification. For the parameter regime relevant to our experiments, however, both are negligible.

Ribbon thickness τ is not typically predicted by the Stefan problem, but must come from solving the fluid flow which limits it. In the case of thin ribbons, a solution is available. It predicts

$$\tau^2 W/\Delta P = \text{function of } \{\bar{V}/U, R/G\}. \quad (19)$$

When combined with eqn (15), ribbon thickness is predicted solely in terms of control parameters. In that sense, the problem has been fully solved. The explicit form of the function in eqn (19) depends on the choice of distinguished limits for the fluid mechanics. One choice delivers the function presented in Carpenter *et al.* [34] where agreement with experiment is exhibited (there, B_s is a fitting parameter, essentially).

In summary, for a parameter regime accessible to experiment, the analysis provides,

(i) precise conditions under which the fluid mechanics and heat transfer decouple;

(ii) an analytic solution of the Stefan problem, which predicts shapes that fall between the linear and quadratic growth forms, and which, in turn, fixes;

(iii) the boundary of the flow domain on which the fluid flow problem must be solved;

(iv) a simple, direct relationship between the heat transfer coefficient and the solidification speed (explicit for thin and implicit for thick ribbons).

Acknowledgements—This work was supported by NSF Grant MSM 8711824 and CTS 90244661. PHS thanks Dr Christian Karcher for contributions to interpreting the Stefan problem and its solution, and the Humboldt Foundation for partial support of Dr Karcher. The authors thank Dr Ho Yu and Dr Men Chu, Alcoa Technical Center, for useful discussions.

REFERENCES

1. Kurz, W. and Fisher, D. J., *Fundamentals of Solidification*, 3rd edn. Trans Tech Publications, Switzerland, 1989, p. 65.
2. Carpenter, J. K. and Steen, P. H., Planar-flow spin-casting of molten metals: process behavior. *Journal of Material Science*, 1992, **27**, 215–225.
3. Davies, H. A., Solidification mechanisms in amorphous and crystalline ribbon casting. In *Rapidly Quenched Metals*, ed. S. Steeb and H. Warlimont. Elsevier Publishers, 1985, pp. 101–106.
4. Gutierrez, E. M. and Szekley, J., A mathematical model of the planar-flow melting spinning process. *Metallurgical Transactions—B*, 1986, **17**, 695–703.
5. Takeshita, K. and Shingu, P. H., An analysis of the heat transfer problem with phase transformation during rapid quenching. *Transactions of the Japan Institute of Metals*, 1983, **24**, 293–300.
6. Clyne, T. W., Numerical treatment of rapid solidification. *Metallurgical Transactions—B*, 1984, **15**, 369–381.
7. Chu, M. G., Giron, A. and Granger, D. A., Microstructure and heat flow in melt-spun aluminum alloys. *Proceedings of the International Conference on Rapidly Solidified Materials*, ASM, 1986, pp. 311–316.
8. Carpenter, J. K. and Steen, P. H., On the heat transfer to the wheel in planar-flow melt-spinning. *Metallurgical Transactions—B*, 1990, **21**, 279–283.
9. Ludwig, A., Frommeyer, G. and Gr'an'asy, L., Mod-

elling of crystal growth during the ribbon formation in planar flow casting. *Process Metallurgy*, 1990, **10**, 467–471.
10. Wang, G.-X. and Matthys, E. F., Numerical modelling of phase change and heat transfer during rapid solidification processes: use of control volume integrals with element subdivision. *International Journal of Heat and Mass Transfer*, 1992, **135**(1), 141–153.
11. Wang, G.-X. and Matthys, E. F., Two-dimensional boundary-layer modeling of planar flow melt-spinning with undercooling. In *Melt-spinning and Strip Casting: Research and Implementation*, ed. E. F. Matthys. The Minerals, Metals and Materials Society, Warrendale, PA, 1992, pp. 263–282.
12. Davies, H. A., Shohodi, N. and Warrington, D. H., The structures of rapidly quenched nickel-based superalloy ribbon produced by melt spinning. In *Rapid Solidification Processing: Principles and Technologies II*, ed. R. Mehrabian, B. A. Kear, and M. Cohen. Claitor's Publishing Division, Baton Rouge, LA, 1981, pp. 153–164.
13. Kukura, J., Ford, K., Singh, A., Steen, P. H. and Ibaraki, T., Measurement of heat transfer coefficient in planar flow casting. In *Simulation of Materials Processing: Theory, Methods and Applications*, ed. S.-F. Shen and P. Dawson. Balkema, Rotterdam, 1995, pp. 1153–1157.
14. Ibaraki, T. and Steen, P. H., Planar-flow casting: puddle dynamics and process behavior. In *Modelling of Casting, Welding and Advanced Solidification Processes VII*, ed. M. Cross and J. Campbell. The Minerals, Metals and Materials Society, 1995, pp. 889–895.
15. Ibaraki, T., Planar-flow melt-spinning: experimental investigation on solidification, dynamics of the liquid puddle, and process operability. M.S. thesis, Cornell University, Ithaca, New York, 1996.
16. Liu, W., Wang, G.-X. and Matthys, E. F., Thermal analysis and measurements for a molten metal drop impacting on a substrate: cooling, solidification and heat transfer coefficient. *International Journal of Heat and Mass Transfer*, 1995, **38**(8), 1387–1395.
17. Turnbull, D., Thermodynamics and kinetics of laser-induced structure changes. In *Physical Processes in Laser-Materials Interactions*, ed. M. Bertollotti. NATO-ASI series, 1983, pp. 117–142.
18. Yu, H., A fluid mechanics model of the planar flow melt spinning process under low Reynolds number conditions. *Metallurgical Transactions—B*, 1987, **18B**, 557–563.
19. Steen, P. H., Yu, H. and Carpenter, J. K., Fluid mechanics of the planar-flow melt-spinning process. *AIChE*, 1988, **34**, 1673–1682.
20. Schlichting, H., *Boundary-Layer Theory*, 7th edn. McGraw-Hill, New York, 1979, p. 506.
21. Hatch, J. E., *Aluminum: Properties and Physical Metallurgy*. American Society for Metals, Metals Park, OH, 1984.
22. Wilde, P. D. and Matthys, E. F., Experimental investigation of the planar flow casting process: development and free surface characteristics of the solidification puddle. *Material Science Engineering*, 1992, **A150**, 237–247.
23. Steen, P. H., Solidification by planar-flow spin-casting. In *Interactive Dynamics of Convection and Solidification*, ed. S. H. Davis, H. E. Huppert, U. Müller and M. G. Worster. NATO ASI series, Kluwer, Netherlands, 1992, pp. 229–231.
24. Carpenter, J. K., Processing of molten metals by planar-flow spin-casting: modelling and experiments. Ph.D. thesis, Cornell University, Ithaca, New York, 1990.
25. Steen, P. H. and Karcher, C., Fluid mechanics of spin-casting of metals. *Annual Review of Fluid Mechanics*, 1997, **29**, 373–397.
26. Devaud, G. and Turnbull, D., Undercooling of liquid germanium. *Material Research Society Symposium Proceedings*, 1987, **57**, 89–97.
27. Porter, D. A. and Easterling, K. E., *Phase Transformations in Metals and Alloys*. Van Nostrand Reinhold, Wokingham, Berkshire, UK, 1981.
28. Geiger, G. H. and Poirier, D. R., *Transport Phenomena in Metallurgy*. Addison-Wesley, Reading, MA, 1973.
29. Yao, L. S. and Prusa, J., Melting and freezing. *Advances in Heat Transfer*, 1989, **19**, 1–95.
30. Kavesh, S., Principles of fabrication. In *Metallic Glasses*. Amer. Soc. of Metallurgists, Metals Park, OH, 1978, pp. 36–73.
31. Hillmann, H. and Hilzinger, H. R., On the formation of amorphous ribbons by the melt-spin technique. In *Rapidly Quenched Metals*, ed. B. Cantor, 1978, pp. 22–29.
32. Jones, H., *Rapid Solidification of Metals and Alloys*. Institution of Metallurgists, London, 1982.
33. Chen, S.-J., Ren, R. C. and Tseng, A. A., Interface heat transfer in metal casting on a moving substrate. *Proceedings of the ASME Winter Annual Meeting*, 1993, pp. 1–8.
34. Carpenter, J. K., Agger, E. C. and Steen, P. H., Fluid mechanics and heat transfer of planar-flow melt-spinning. In *Modeling of Casting and Welding Processes V*, ed. M. Rappaz, M. R. Ozgu and K. W. Mahin. The Minerals, Metals and Materials Society, Warrendale, PA, 1991, pp. 621–627.